Journal of Colloid and Interface Science **223,** 167–178 (2000)
doi:10.1006/jcis.1999.6638, available online at http://www.idealibrary.com on IDEAL®

Formation of Layered Single- and Double-Metal Hydroxide Precipitates at the Mineral/Water Interface: A Multiple-Scattering XAFS Analysis

Andreas C. Scheinost[1] and Donald L. Sparks

University of Delaware, Newark, Delaware 19717

E-mail: scheinos@udel.edu

Received February 4, 1999; accepted November 23, 1999

Spectroscopic and microscopic studies have shown that Ni and Co sorption by clay minerals may proceed via formation of surface precipitates. Several studies employing X-ray absorption fine structure (XAFS) spectroscopy suggested the formation of turbostratic, α-type metal hydroxides, of layered double hydroxides (LDH) with Al-for-metal substitution, and of 1 : 1 or 2 : 1 phyllosilicates. Distinction of these phases is difficult because they have low crystallinity and/or a small mass compared to the sorbents, and because they have similar metal–metal distances in their hydroxide layers/sheets. Distinction of these phases is crucial, however, because they have substantially differing solubilities. In this paper we show that an XAFS beat pattern at about 8 Å^{-1} can be used as a fingerprint to unequivocally distinguish LDH from the α-type hydroxides and phyllosilicates. Full multiple-scattering simulations and experimental spectra of model compounds indicate that the beat pattern is due to focused multiple scattering at Me/Al ratios between 1 and 4 (Me = Ni, Co). By applying the fingerprint method to new and to already published XAFS data on Ni and Co surface precipitates, we found that LDH preferentially forms in the presence of the Al-containing sorbents pyrophyllite, illite, kaolinite, gibbsite, and alumina above pH 7.0. However, α-type metal hydroxides form in the presence of the Al-free sorbents talc, silica, and rutile, and in the presence of the Al-containing clay minerals montmorillonite and vermiculite. We believe that the high permanent charge of these latter minerals prevents or retards the release of Al. When Al is available, the formation of LDH seems to be thermodynamically and/or kinetically favored over the formation of α-type hydroxides.

Key Words: **sorption; surface precipitation; layered double hydroxide; hydrotalcite; α-Ni hydroxide; X-ray absorption spectroscopy.**

INTRODUCTION

Sorption reactions at the mineral/water interface largely determine the mobility and bioavailability of metals in soils and sediments. Recent studies using spectroscopic and microscopic techniques have shown that the formation of metal precipitates is far more important for the removal of metals from solution than previously thought (1–4). The reaction of Ni and Co with a variety of surfaces has received considerable attention because of the geochemical distribution and environmental toxicity of these elements (5–17) and their importance in industrial catalysis (18–23). *In situ* XAFS spectroscopy has shown that Ni- and Co-containing precipitates form within short reaction times (minutes to days) in the presence of clay minerals, even when the calculated surface coverage is below a monolayer, and the pH is below saturation with respect to the known solubility products of β-type hydroxides (2, 24–32). However, the identity of these precipitates, which is essential to derive thermodynamic properties and to predict the fate of Ni and Co in the environment, is still debated. Therefore, the goal of this paper is to improve the spectroscopic identification of these precipitate phases.

The principal feature common to all the precipitates as identified by XAFS is an Me–Me distance which is contracted in comparison to those of the β-type metal hydroxides (2, 15, 24–31). This contraction has been explained by five different mechanisms:

(1) Epitaxial growth on the surface of a sorbent (33). As $Me(OH)_6$ octahedra based on Ni or Co are larger than those based on Al, layers of Ni or Co octahedra would have to contract to fit onto surface structures whose dimensions are determined by Al octahedra (e.g., 1 : 1 and 2 : 1 phyllosilicates, gibbsite). A possible mechanism is the epitaxial growth at the reactive, amphoteric edge sites of a sheet of Al octahedra where strong bonds between the sorbent and the sorbate may develop via inner-sphere complexation (15, 33). However, epitaxial growth on the planar sites of sheets of Al octahedra is unlikely, because bonds between these sites and the precipitates would not be strong enough to transfer the strain force necessary to shrink metal octahedra (34).

(2) Structural defects. Cation vacancies due to defects in the crystal structure may cause a lattice contraction (29, 33).

(3) Formation of a phyllosilicate with one or two silica sheets sandwiching a metal hydroxide sheet (34). Investigation of a number of Ni silicates showed that the Ni–Ni distances were

[1] To whom correspondence should be addressed. Current address: Institute of Terrestrial Ecology, Swiss Federal Institute of Technology—ETHZ, Grabenstrasse 3, 8952 Schlieren, Switzerland.

0021-9797/00 $35.00

smaller than those of β-Ni hydroxide (9). This contraction has been explained by a size mismatch between the Ni hydroxide sheet and the one or two adjacent silica sheets which are connected by strong bonds via corner sharing of ligands (34).

(4) Coprecipitation of the larger Ni or Co with the smaller-sized Al by forming LDHs similar to minerals of the hydrotalcite subgroup (26, 27, 29, 30, 33). The resulting net positive layer charge is balanced by interlayer anions.

(5) Formation of metastable, α-type Ni or Co hydroxides (29, 35). These layered single hydroxides can host a range of different anions in the variable interlayer space (36) and may be structurally very similar to LDH (37). A net positive layer charge may be created by hydroxyl vacancies (36) or by the protonation of hydroxyls (37).

Each of these mechanisms, alone or in combination, may explain the observed contraction of metal–metal distances. The dissolution of an Al-containing sorbent is a prerequisite for the contraction by epitaxial growth (1) or by formation of LDH (4), and the presence of Si is a prerequisite for the formation of phyllosilicate (3). However, contraction of Co–Co distances has also been observed in precipitates formed in the presence of the Al- and Si-free mineral rutile (27), which indicates that the formation of α-type hydroxide (5) or another structure with structural defects in the form of cation vacancies (2) is the most likely explanation in this case. Using optical spectroscopy, Scheinost *et al.* (35) showed that Ni–O distances are shorter in precipitates formed in the presence of the Al-containing minerals, pyrophyllite and gibbsite, relative to precipitates formed in the presence of talc and amorphous silica. In the presence of an Al source, the Ni–O bond distances were in agreement with Ni–Al LDH, and in the absence of an Al source, they were in agreement with α-Ni hydroxide (35).

However, the unequivocal discrimination of the surface precipitates by fitting XAFS spectra seems to be hindered by three limitations. First, Me–Me distances of candidate phases like α-type hydroxides, Me–Al LDH, and phyllosilicates are very similar and may be difficult to distinguish by XAFS (25, 35). Furthermore, in spite of similar Me–Me distances, surface precipitates may structurally differ from candidate phases grown in solution rather than in mineral suspensions. Second, the existence of Al in the structure of the precipitates, which would indicate the formation of LDH, was evidenced only indirectly by an improved fit after adding an Al shell (28, 30). Due to the similar distances of Co and Al in Co–Al LDH, or of Ni and Al in Ni–Al LDH, and the weak backscattering of Al versus Co or Ni, however, this improvement may be the consequence of having more degrees of freedom rather than proof for the substitution itself. Third, the existence of a third metal shell at about twice the distance of the first shell proves the existence of a brucite-like hydroxide sheet (25, 29, 33); as this is a common structure element of all the candidate phases, it does not discriminate between them.

D'Espinose de la Caillerie and co-workers indicated that several beat patterns in the XAFS spectra of Ni–Al LDH samples might be characteristic fingerprints for this phase (26, 38). We found that one of these beat patterns, occurring at about 8 $Å^{-1}$, is strong enough to be detectable also in the much noisier spectra of surface precipitates. The beat frequently coincides with precipitate formation in the presence of an Al-containing phase, suggesting that it may be diagnostic for Al substitution in Ni and Co hydroxide. We verified this hypothesis by a triple approach. First, we measured XAFS spectra of *Ni model compounds* with known structure and composition, representing possible precipitate phases. Second, we performed ab initio *multiple-scattering simulations* of model structures to improve our understanding of the experimental XAFS spectra. Third, we compared XAFS spectra of *Ni surface precipitates* growing in Al-free and Al-containing environments by using Al-free (talc, amorphous silica) and Al-containing sorbents (pyrophyllite and gibbsite). This allowed us to verify the sensitivity of the diagnostic feature at 8 $Å^{-1}$. Finally, the use of this easily detectable fingerprint, which complements information provided by XAFS fits, enabled us to reinterpret XAFS spectra of Co- or Ni-containing precipitates which have been published within the last decade.

In the following we will use the expression *sorption* for any surface-mediated removal of ions from solution, including adsorption and precipitation mechanisms. The precipitates formed this way will be called surface precipitates, although they may not be attached to the sorbent (29). Correspondingly, we will use the unit *surface density* as a unifying measure of sorbate/sorbent ratios without implying an even distribution of the sorbate across the sorbent surface.

MATERIALS AND METHODS

Synthesis of Ni Model Compounds

An α-Ni hydroxide was prepared by adding 550 mL of 30% ammonia to 500 mL of 1 M $Ni(NO_3)_2$ (36). The solution was vigorously stirred and purged with N_2. After 2 h, the suspension was centrifuged and washed with D.I. water in 5 cycles, shock-freezed in liquid N_2, and freeze-dried. A β-Ni hydroxide sample was prepared by using the same precipitation method as above, but the suspension was aged under N_2 atmosphere at room temperature for 4 weeks. This sample was then washed and freeze-dried like the α-Ni hydroxide.

Two Ni–Al LDH samples (labeled LDH Ni/Al = 1.3 and LDH Ni/Al = 4.3, respectively) were prepared by controlled hydrolysis (39). The amounts of Ni and Al (added as $Ni(NO_3)_2 \cdot 9H_2O$ and $Al(NO_3)_3 \cdot 9H_2O$) were adjusted to give initial Ni/Al ratios in solution of 2 and 10, respectively. Under vigorous stirring, 450 mL of both solutions were combined. The pH was raised to 6.9 by addition of 2.5 M NaOH and then kept constant for 5 h using an autotitrator. The precipitate was washed and dried as before. Metal solutions were purged with N_2, and the 2.5 M NaOH was freshly prepared to minimize carbonate uptake by the precipitate. By acid digestion, Ni/Al ratios of 1.3 and 4.3 were determined, indicating a preferential uptake of Al from solution during precipitation. A Ni phyllosilicate was prepared

according to Grauby *et al.* (40) by hydrothermally aging the initial precipitate at 150°C for 2 weeks.

Ni Sorption on Pyrophyllite, Gibbsite, Talc, and Silica

The N_2-BET surface areas of the sorbent phases used in this study are 95 $m^2\ g^{-1}$ for pyrophyllite, 75 $m^2\ g^{-1}$ for talc, 25 $m^2\ g^{-1}$ for gibbsite, and 90 $m^2\ g^{-1}$ for the amorphous silica (Zeofree 5112, Huber Company). The mean particle size of the amorphous silica is 10 μm (Microtrac method); the particle size of the other sorbents is <2 μm (Stokes diameter). X-ray diffraction (XRD) showed minor impurities of kaolinite and quartz in pyrophyllite, about 10% bayerite in the gibbsite, and about 20% chlorite in talc, while the amorphous silica was pure. After acid digestion, an Al/Mg ratio of 0.01 was determined by ICP-AES for the talc sample, confirming its low Al content. Therefore, even with these impurities, the classification of the sorbents in Al-rich (pyrophyllite, gibbsite) and Al-poor (talc, silica) is valid. The preparation of the sorbents was as described in Scheidegger *et al.* (28, 31).

Experiments were run at pH 7.5 and 23°C in a background electrolyte of 0.1 M $NaNO_3$. A total Ni concentration of 1.5 m M was used along with a solids concentration of 5 g L^{-1}. The systems were either slightly oversaturated ($\Omega = 1.08$) or undersaturated with respect to β-Ni hydroxide, depending on which solubility constant was used. Solubility constants reported for β-Ni hydroxide ranged from $\log K = -10.8$ to $\log K = -18$ (41). Solubility constants for α-Ni hydroxide or Ni–Al LDH are not available to the best of our knowledge. The sorbents were hydrated in the background electrolyte for 24 h on a reciprocal shaker. The pH of the suspensions was then adjusted to 7.5 using a pH stat apparatus. They were vigorously stirred with a magnetic stir bar and purged with N_2 to eliminate CO_2. After 2 h, an appropriate amount of Ni from a 0.1 M $Ni(NO_3)_2$ stock solution was added in three steps within a 2-min period to avoid temporal and local oversaturation with respect to β-Ni hydroxide. The pH was controlled for 2 to 4 days by the pH stat (± 0.05 units) followed by manual adjustments (± 0.2 units) for the subsequent aging periods. After the desired reaction period, aliquots of the suspension were collected and immediately centrifuged at 14000 rpm and 2°C. The supernatant was passed through a 0.22-μm membrane filter and analyzed for Ni, Si, Al, and Mg by ICP-AES. Ni sorption was calculated from the difference between the initial and the final Ni concentrations. The remaining wet pastes were washed once with 0.1 M $NaNO_3$ to remove excess Ni in the entrained electrolyte. The samples were analyzed by XAFS immediately after sampling (the 2-h Ni-pyrophyllite sample) or after storage at 2°C for up to 4 weeks (all other samples).

XAFS Data Collection

X-ray absorption spectra were collected at beamline X-11 A at the National Synchrotron Light Source, Brookhaven National Laboratory, Upton, NY. The electron storage ring operated at 2.5 GeV with a beam current between 120 and 240 mA. The beam height was adjusted to 0.5 mm before it entered the Si(111) crystal monochromator. Higher order harmonics were suppressed by detuning the monochromator by 25%. The monochromator position was calibrated by assigning the first inflection point on the K-absorption edge of metallic nickel foil to 8333.0 eV. Fluorescence spectra were collected using an Ar-filled Stern–Heald detector with Soller slits and a Co-3 filter (42). The incoming beam was measured with an N_2-filled ion chamber. The samples were oriented at a 45° angle to the incident beam and cooled to 77 K by using a cold finger to reduce thermal disorder. Samples run for comparison at room temperature resulted in noisier spectra but did not show alterations of the sorbed phases due to the freezing (31). Wet pastes of Ni-reacted minerals and dry powders of model compounds diluted in corundum (Buehler's Micropolish) were mounted in Al holders and covered with Mylar windows. Scans were collected in triplicate using the following parameters (photon energies relative to the edge of Ni foil): -200 to -30 eV in 10 eV steps and 1 s counting time per step; -30 to 30 eV in 0.5 eV steps at 1 s each step; 30 eV to 14.5 $Å^{-1}$ in 0.07 $Å^{-1}$ steps at 5 s.

XAFS Data Analysis

All steps of the XAFS data reduction were performed using the WinXAS 97 1.1 software package (43). The spectra were normalized by fitting second-degree polynomials to the pre-edge and post-edge regions. The position of the pre-edge peak of Ni^{2+} was used to check for energy shifts between single scans before averaging. The energy axis (eV) was converted to photoelectron wave vector units ($Å^{-1}$) by assigning the origin, E_0, to the first inflexion point of the absorption edge. The XAFS backscattering signal was isolated from the absorption edge background by using a cubic spline function with 5 segments. The resulting $\chi(k)$ functions were weighed by k^3 to account for the damping of oscillations with increasing k and were Fourier-transformed to achieve radial structure functions (RSF). A Bessel window with a smoothing parameter of 4 was used to suppress artifacts due to the finite Fourier filtering range between 1.5 and 14.5 $Å^{-1}$.

Theoretical scattering paths were calculated with FEFF 7.02 (44), using the structure of lizardite where Ni was substituted for Mg in octahedral positions (45). Further modifications of the structure to simulate a range of elemental compositions and vacancies are described below. Scattering paths out to 8 Å were calculated using an amplitude reduction factor, S_0^2, of 0.85. Fits were performed in R space over the range of the first two shells (1.1 to 3.4 Å). To reduce the number of adjustable parameters, S_0^2 was fixed at 0.85 (25). The deviation between the fitted and the experimental spectra is given by the relative percentage of residual, %Res.

FEFF Simulations

Candidate phases for metal (Me) precipitates (Me = Ni or Co) that may form in the presence of the sorbents used in this study are α-Me hydroxide, Me–Al LDH, and 1 : 1 or 2 : 1 phyllosilicates (26, 34, 35). The basic structural component of these compounds is a metal hydroxide sheet consisting of edge-sharing

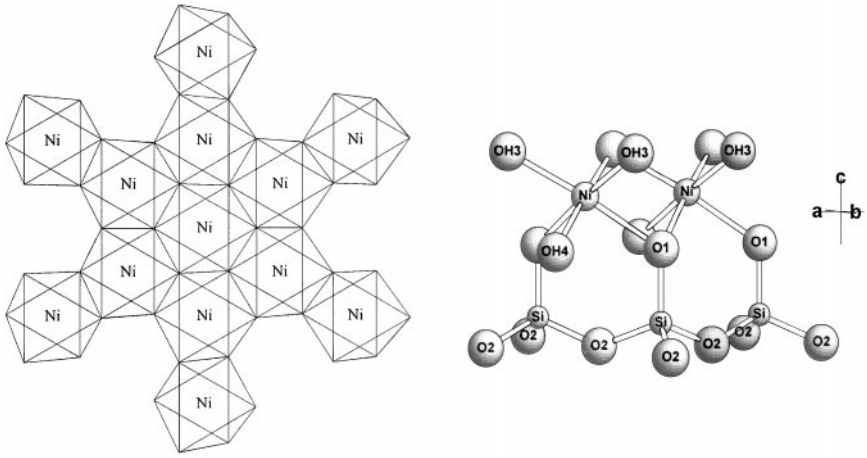

FIG. 1. The local structure of lizardite (45), a 1 : 1 phyllosilicate, which is used to simulate the structure of Ni and Co surface precipitates. Left: A central Ni atom with its first-shell and third-shell Ni neighbors in the brucite-like Ni hydroxide sheet (001). All Ni atoms are separated by 3.08 Å along the hexagonal axes. Right: Cross section of the 1 : 1 layer, consisting of one octahedral sheet hosting Ni and one tetrahedral sheet hosting Si. Each Ni atom has two Si neighbors at 3.29 Å. Omitting the tetrahedral sheet creates the basic layer of α-Ni hydroxide; substituting Al for Ni creates the positively charged layer of Ni–Al layered double hydroxide, LDH.

octahedra (Fig. 1). In both α-Me hydroxide and Me–Al LDH, the hydroxide layers are separated by layers of anions, resulting in a d-spacing of about 7 to 8 Å when nitrate and carbonate are the interlayer anions (36, 39). The phyllosilicate structures have one or two silicate sheets attached to the hydroxide sheets, resulting in a d-spacing of 7 Å (1 : 1 phyllosilicates) or 9 Å (2 : 1 phyllosilicates) in close stacking (46).

To simulate the XAFS spectra of these compounds, we used the structure of the 1 : 1 Mg phyllosilicate lizardite (45) (Fig. 1), where distances of 3.08 Å between octahedral centers are similar to those of α-Ni hydroxide ($R_{\text{Ni–Ni}} = 3.08$ Å) (47) and Ni–Al LDH ($R_{\text{Ni–Ni}} = 3.06$ Å) (26). The Si atoms in the attached silica sheet are 3.29 Å apart from the octahedral centers, similar to the distances found in Co and Ni phyllosilicates (34) (Fig. 1). By substituting Mg atoms by Ni and Al we created Ni and Ni–Al phyllosilicates. Omitting the Si atoms and one row of O atoms (labeled O2 in Fig. 1) produced the respective α-type and LDH structures. Furthermore, Ni atoms were partially omitted to create vacancies. Clusters for the corresponding Co model compounds were constructed in a similar way. To account for the larger Co^{2+}, we isotropically enlarged the basic structure of lizardite by 1%, yielding the $R_{\text{Co–Co}}$ of 3.10 Å usually observed for Co precipitates (26, 33). Theoretical scattering paths were calculated with FEFF 7.02 assuming a random orientation of particles with respect to the polarization vector of the incident beam (44). We chose a cluster radius of 8 Å and an amplitude reduction factor, S_0^2, of 0.85 (25). The Debye–Waller factors (σ^2), accounting for atomic disorder, were set at zero. The large number of paths resulting from a cluster of 177 atoms was restricted by allowing only paths with a maximum of 5 legs and an amplitude of at least 2% of the largest amplitude (which was that of either the first, Ni–O, or the second, Ni–Ni, coordination shell). Depending on the elemental composition, the number of paths varied between 140 and 210.

RESULTS AND DISCUSSION

Characterization of Model Ni Compounds

The XRD patterns and FTIR spectra shown in Fig. 2 confirm the phase identity of the model compounds (23, 36, 39, 40, 48). The XRD patterns of α-Ni hydroxide, the two LDH samples, and the Ni phyllosilicate show asymmetric $hk0$ peaks indicative of a turbostratic layer structure. The β-Ni hydroxide has a d-spacing of 4.6 Å, consistent with a close packing of hydroxide layers, while the d-spacing of α-Ni hydroxide and the LDH samples is >7.7 Å, indicative of interlayers >3.1 Å (Table 1). Both LDH samples show strong nitrate bands at 1384 cm^{-1}, indicating that the interlayer space is occupied by nitrate anions which could not be removed by the repeated washings with D.I. water (Fig. 2). These nitrate peaks are strongly enhanced by the use of KBr pellets (49). The α-Ni hydroxide sample has strong nitrato (-ONO_2) bands at 1309 and 1479 cm^{-1} in addition to the nitrate band, indicating that part of the nitrate forms covalent bonds with the hydroxide layers (26). The nitrate and nitrato bands of β-Ni hydroxide may be explained by an α-Ni hydroxide impurity due to incomplete transformation from its α-Ni hydroxide precursor. Such a low-crystalline impurity would not be detectable by XRD due to masking by the strong XRD

TABLE 1
XRD of Ni Model Compounds

	d-spacing (Å)	110 (Å)
β-Ni hydroxide	4.6	—
α-Ni hydroxide	8.0	1.55
Ni phyllosilicate	10.4	1.53
LDH Ni/Al = 1.3	7.7	1.52
LDH Ni/Al = 4.3	8.0	1.50

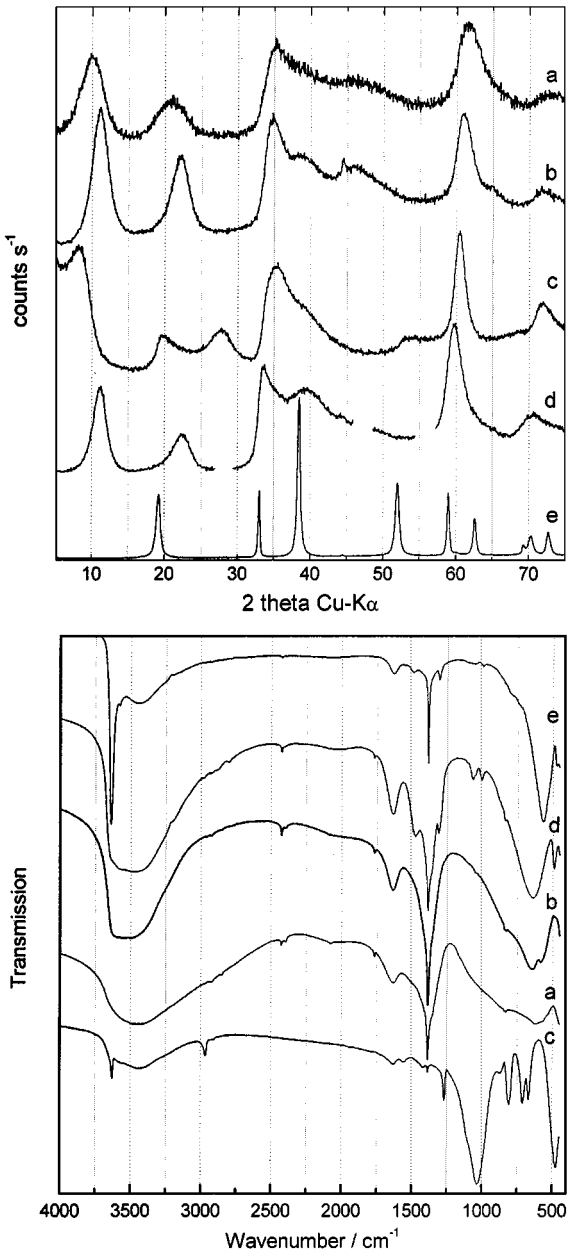

FIG. 2. Powder X-ray diffraction patterns (top) and FTIR spectra (bottom) of Ni reference compounds: (a) LDH Ni/Al = 1.3, (b) LDH Ni/Al = 4.3, (c) Ni phyllosilicate, (d) α-Ni hydroxide, (e) β-Ni hydroxide.

pattern of β-Ni hydroxide (Fig. 2). The Ni phyllosilicate sample shows a very weak nitrate band which may be due to incomplete silicate-for-nitrate exchange. The position of the OH stretching band at 3629 cm^{-1}, the SiO stretching band at 1031 cm^{-1}, the doublet at 667–708 cm^{-1}, and the XRD layer spacing of 10.4 Å are all consistent with an Ni talc-like phase (21).

The position of the 110 diffraction peak (at ca. 60° 2θ) depends on the unit-cell dimensions along the *a* and *b* axes, i.e., along the planar extensions of the hydroxide layers, and is indicative of metal–metal distances in this layer. This peak is at 1.55 Å for the unsubstituted α-Ni hydroxide, but it decreases with decreasing Ni/Al ratio, corroborating that the smaller Al^{3+} substitutes for the larger Ni^{2+} (Table 1). This dimension is also smaller for the Ni phyllosilicate sample, which has been explained by the size mismatch between the octahedral Ni hydroxide sheet and the tetrahedral silica sheet and by the greater potential of the octahedral sheet for the necessary size adjustment (34, 50).

In Fig. 3, the unfiltered $\chi(k)k^3$ spectra and the corresponding radial structure functions (RSFs) of the α-Ni hydroxide sample are shown in comparison with the Ni–Al LDH samples (top) and the Ni phyllosilicate sample (bottom). All RSFs (which are uncorrected for phase shift) show two strong peaks, the first at 1.7 Å indicative of backscattering from the first ligand shell, and the second at 2.7 Å indicative of backscattering from the first metal shell.

The intention of our study was to develop a method which allows for an unequivocal discrimination of several possible surface precipitate phases by XAFS. Therefore, we fitted the XAFS spectra of the 5 model compound samples without using the a priori knowledge provided by the method of synthesis, acid digestion, XRD, and FTIR—information which does not exist for the surface precipitates. For all model compounds, we achieved reasonable fits ($\chi^2_{res} \leq 9.0\%$) of the two main RSF peaks (1.1 Å $\leq R \leq$ 3.4 Å) by using one Ni–O and one Ni–Ni path (Table 2). The relatively large error for sample LDH Ni/Al = 1.3 derives from the O shell, which may indicate a higher distortion of the $Ni(OH)_6$-octahedra due to the higher Al content of this sample (Fig. 4, top). The real part of the second shell is well fit by one Ni path, while the imaginary part shows some deviation around 2 Å. The fit of this region was improved by including an Al path (Fig. 4, bottom). Reasonable fit parameters could be derived by correlating R_{Ni-Ni} and R_{Ni-Al} (Table 2). However, the fit of the Al-free α-Ni hydroxide was also improved by adding an Al path (not shown). Thus, the fit improvement after addition of an Al shell is clearly not proof for the existence of this shell.

The Ni–O distances of the reference compounds varied between 2.04 and 2.06 Å, showing no significant variation beyond the experimental error of 0.01–0.02 Å (25). The Ni–Ni distances (R_{Ni-Ni}) decrease in the order β-Ni hydroxide > α-Ni hydroxide > Ni silicate > LDH. The R_{Ni-Ni} of 3.12 Å for β-Ni hydroxide is identical to the one derived from neutron diffraction (51) and XAFS (47). The R_{Ni-Ni} of 3.09 Å for α-Ni hydroxide is consistent with the range 3.07 to 3.09 Å found by Pandya *et al.* (47). In a recent XAFS study, Mansour and Melendres claimed an R_{Ni-Ni} of 3.12 Å for a so-called α-Ni hydroxide (52). However, XRD of this sample revealed *h*00 and 0*k*0 peaks similar to that of β-Ni hydroxide, but with larger *d*-spacing (Mansour, personal communication), which is indicative of an α-β-Ni hydroxide intermediate (53, 54). Compared to the other two compounds shown in Fig. 3, the amplitude of the first ligand shell of α-Ni hydroxide is substantially lower, resulting in a CN_{Ni-O} of 5.4 (Table 2). This supports the existence of hydroxyl vacancies,

TABLE 2
XAFS Fit Results of Reference Compounds (Top) and Ni-Reacted Clays (Bottom)

	CN_{Ni-O}[a]	R_{Ni-O}[b] (Å)	σ^2_{Ni-O}[c] (Å^2)	CN_{Ni-Ni}[a]	R_{Ni-Ni}[b] (Å)	σ^2_{Ni-Ni}[c] (Å^2)	CN_{Ni-Al}[a]	R_{Ni-Al}[b] (Å)	σ^2_{Ni-Al}[c] (Å^2)	ΔE_0[d] (eV)	χ^2_{res}[e] %
β-Ni hydroxide	6.5	2.06	0.0039	6.3	3.12	0.0040				1.5	5.0
α-Ni hydroxide	5.5	2.04	0.0045	5.6	3.09	0.0060				0.8	5.9
Ni phyllosilicate	6.2	2.06	0.0042	7.0	3.07	0.0031				3.6	7.4
LDH Ni/Al = 1.3	5.4	2.05	0.0036	2.8	3.06	0.0042				0.9	9.0
LDH Ni/Al = 1.3	5.7	2.05	0.0039	3.5	3.06	0.0047	1.4	3.05	0.0046	1.0	7.6
LDH Ni/Al = 4.3	5.7	2.05	0.0047	3.8	3.06	0.0043				0.0	5.1
Ni + talc 4 months	6.3	2.05	0.0052	5.1	3.08	0.0045				0.8	7.4
Ni + silica 1 months	6.5	2.06	0.0050	6.5	3.09	0.0035				1.2	7.9
Ni + gibbsite 4 months	6.4	2.04	0.0044	3.0	3.05	0.0026				−0.1	6.5
Ni + pyrophyllite 2 h	6.5	2.05	0.0043	2.7	3.06	0.0044				0.5	8.3
Ni + pyrophyllite 1 month	6.0	2.05	0.0039	3.7	3.06	0.0040				0.2	5.6
Ni + pyrophyllite 4 months	5.9	2.05	0.0036	3.2	3.06	0.0029				0.6	5.5
Ni + pyrophyllite 12 months	6.0	2.05	0.0049	3.8	3.07	0.0051				0.2	5.0

[a] Coordination number, standard deviation $<\pm 0.05$.
[b] Radial distance, standard deviation $<\pm 0.005$ Å.
[c] Debye–Waller factor, standard deviation $<\pm 5 \times 10^{-5}$ Å^2.
[d] Phase shift.
[e] Deviation between experimental data and fit.

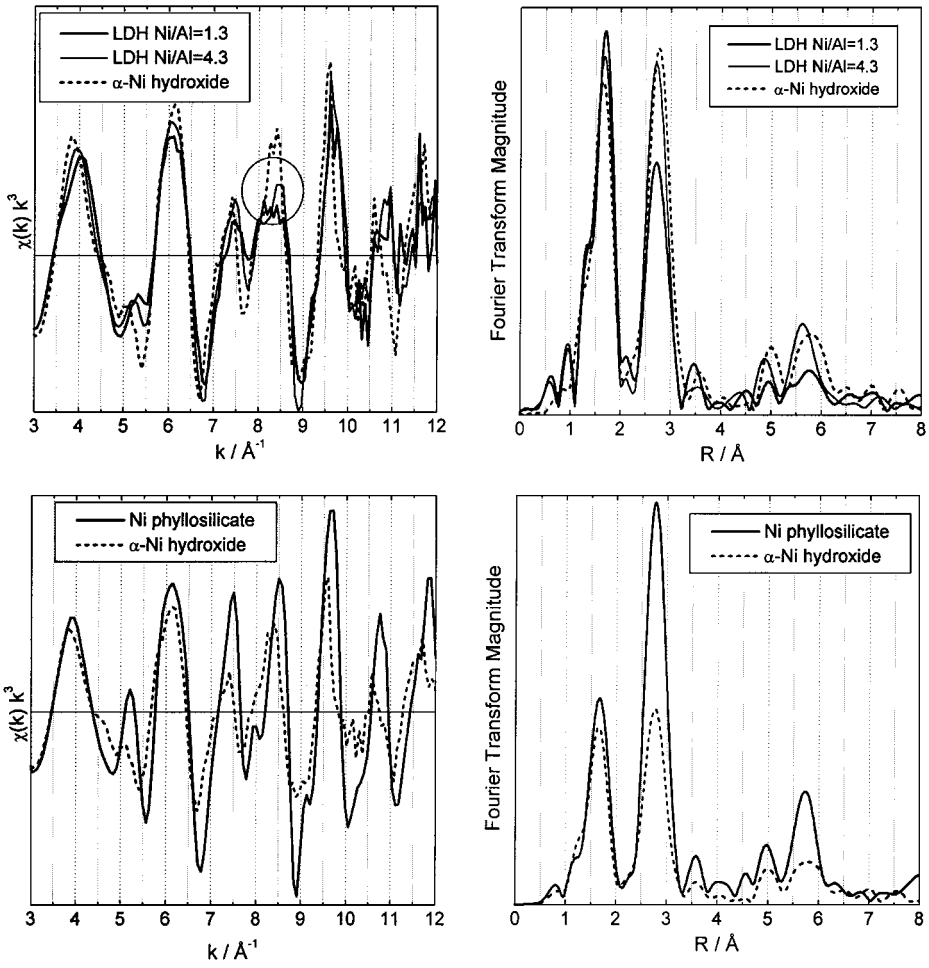

FIG. 3. Experimental $\chi(k)$ functions and RSF of Ni reference compounds. The α-Ni hydroxide sample is shown in comparison with the two LDH samples (top) and the Ni phyllosilicate sample (bottom).

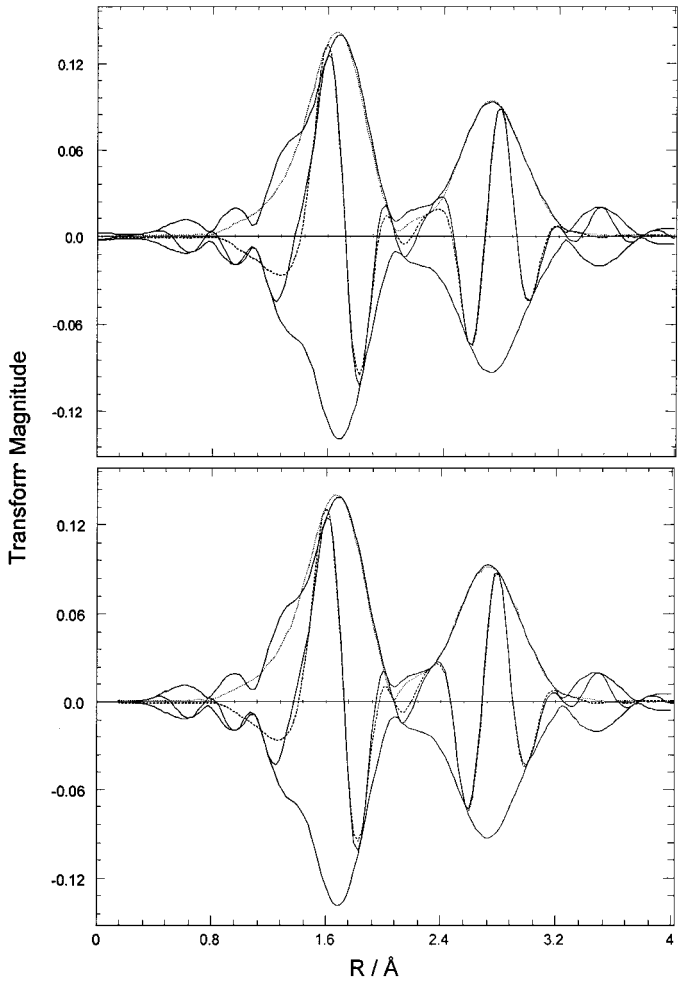

FIG. 4. Comparison of fitting the RSF of sample LDH Ni/Al = 1.3 with (top) and without (bottom) an Al path (in addition to the O and Ni paths). Experimental data are shown in full lines, fit data in hatched lines.

which have been suggested as a source of the net positive charge of α-Ni hydroxide (36). However, protonation of hydroxyl ions may be an additional source of positive charge (37).

The $R_{\mathrm{Ni-Ni}}$ of Ni silicate is smaller than that of α-Ni hydroxide, consistent with XRD and XAFS measurements of Ni-hosting phyllosilicates (Table 2) (55). The $\mathrm{CN_{Ni-Ni}}$ is significantly greater than 6 due to the constructive interference of Si in the tetrahedral sheets at a distance of 3.24 Å. The two LDH samples have the smallest $R_{\mathrm{Ni-Ni}}$, of 3.06 Å, due to Al substitution. However, XAFS is not sensitive enough to show the difference in Al substitution between the two samples as observed by XRD (see above). Due to the partial Ni-for-Al substitution and the destructive interference between both cations occupying the same position (Fig. 5a), the $\mathrm{CN_{Ni-Ni}}$ of 3 is far below the value of 6 expected for full site occupancy. The fit of a second metal shell with Al at the same radial distance as Ni resulted in a combined $\mathrm{CN_{Ni-Ni}}$ and $\mathrm{CN_{Ni-Al}}$ of 4.9. The deviation between the fitted and the experimental spectrum decreased by 20% (see χ_{res}% in Table 2). The $R_{\mathrm{Ni-O}}$ and $R_{\mathrm{Ni-Ni}}$, however, were not influenced by accounting for Al.

In conclusion, all four reference compounds may be distinguished by combining the information on $R_{\mathrm{Ni-Ni}}$ and $\mathrm{CN_{Ni-Ni}}$ provided by XAFS. For the identification of surface precipitates, however, information on $R_{\mathrm{Ni-Ni}}$ and $\mathrm{CN_{Ni-Ni}}$ is not sufficient. A $\mathrm{CN_{Ni-Ni}}$ below 6 may not only be due to (1) the formation of Ni–Al LDH but may also be caused by (2) nanoscale crystallites with a large amount of neighborless Ni atoms, (3) a large amount of cation vacancies, or (4) the presence of (sorbed) mononuclear Ni in addition to the precipitate phase. Furthermore, it cannot be excluded that the $R_{\mathrm{Ni-Ni}}$ of 3.06 Å may also be caused by structural disorder of an Al-free phase, or by the epitaxial growth of an Al-free precipitate on top of an Al-containing sorbent. Thus, further evidence is necessary to prove that Ni–Al LDH is indeed the surface precipitate observed on clay minerals.

The $\chi(k)$ spectra of the LDH samples reveal a distinctive beat pattern between 8.0 and 8.5 $\mathrm{Å}^{-1}$ (circle in Fig. 3). While the other reference compounds show an elongated upward oscillation ending in a sharp tip at ca. 8.5 $\mathrm{Å}^{-1}$, this oscillation seems to be truncated for Ni–Al LDH. Fourier back transformation of the RSF of Ni–Al LDH within $1.1 < R < 3.4$ Å revealed that the beat pattern is not reproduced by the first ligand and first metals shells which are commonly fitted (Fig. 6). The beat pattern appeared, however, when the RSF was back-transformed within $1.1 < R < 6.4$ Å, suggesting that it originates from multiple-scattering paths. Other workers have performed fits for this region, but due to the simplifications necessary to keep the degrees of freedom low, no substantial gain in information on Al-substitution could be derived (33). Therefore, we employed full multiple-scattering simulations to investigate the origin of the beat pattern at 8.0–8.5 $\mathrm{Å}^{-1}$ and to investigate its usefulness for phase characterization.

XAFS Simulations

In Fig. 5 results from the XAFS simulations performed with FEFF7 are assembled. Figure 5b shows the effect of increasing Al-for-Ni substitution in α-Ni hydroxide. In line with the anticyclic single-scattering waves of Ni and Al (Fig. 5a), the superposition of all paths out to 8 Å shows the expected general decline in amplitude as the Al-substitution increases. There are, however, two exceptions: at $k = 8$ $\mathrm{Å}^{-1}$ and at $k = 11.5$ $\mathrm{Å}^{-1}$, upward oscillations are enhanced with increasing substitution (arrows in Fig. 5b). At 50% substitution, the oscillations at 8.5 and 8 $\mathrm{Å}^{-1}$ have roughly the same height, which favorably compares to the filtered spectrum of LDH Ni/Al = 1.3 (Fig. 6). The filtered spectrum of LDH Ni/Al = 4.3 is close to the simulated spectrum at 33% substitution. Thus, the XAFS simulations correctly reproduced all major changes in the experimental spectra from α-Ni hydroxide over LDH Ni/Al = 4.3 to LDH Ni/Al = 1.3.

Filtering the experimental $\chi(k)$ functions of the two LDH samples by Fourier back-transforms showed that the observed beat pattern originates from paths with lengths of about 6 Å (Fig. 6). In general, paths beyond 4 Å do not substantially

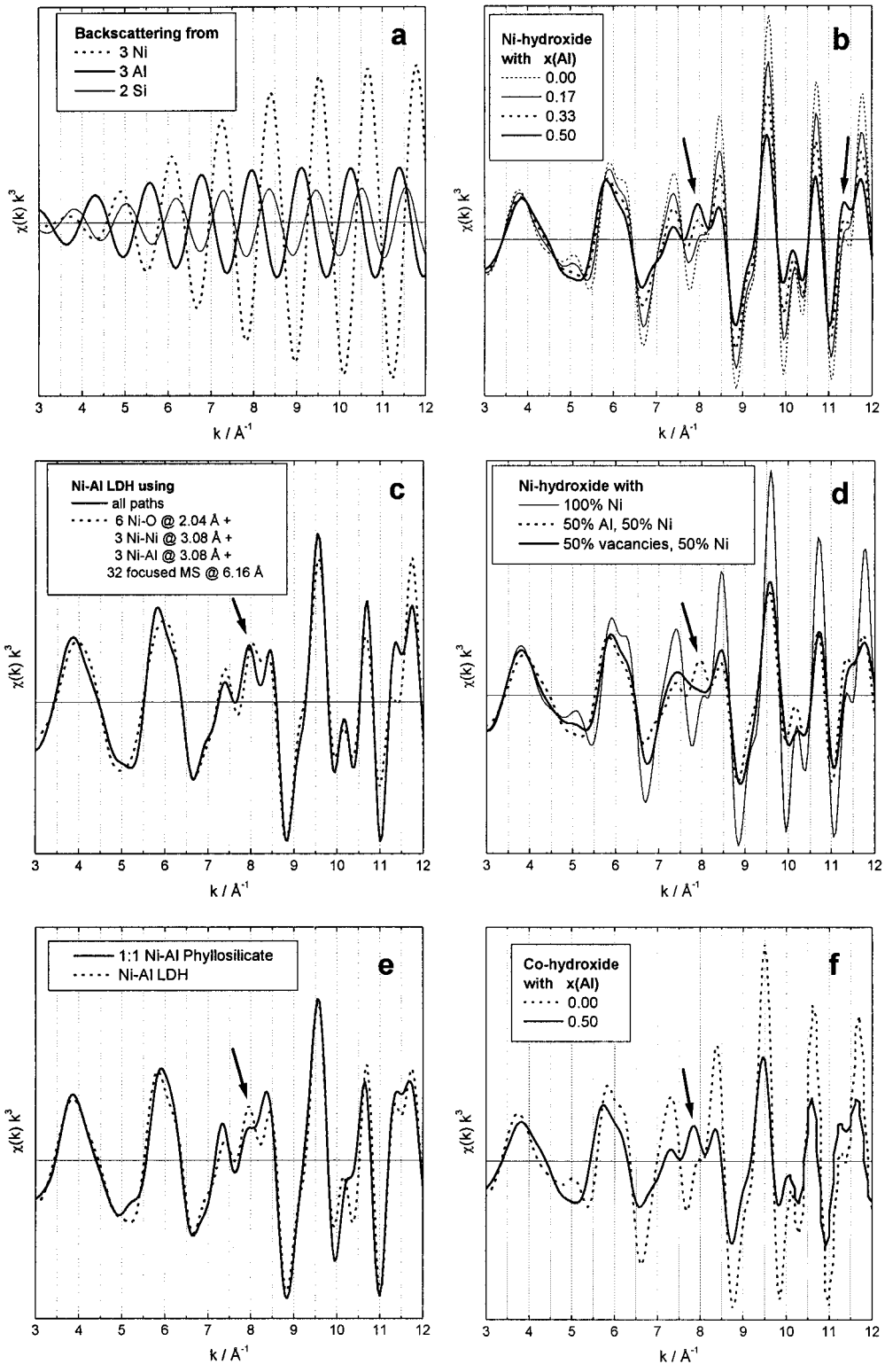

FIG. 5. FEFF simulations based on the structure of lizardite (Fig. 1): (a) single-scattering paths from nearest-neighbor Ni, Al, and Si; (b) effect of Ni-for-Al substitution in an Ni hydroxide layer, modeling the transition from α-Ni hydroxide to Ni–Al LDH; (c) simulation of Ni–Al LDH with $x = 0.50$ superposing all single- and multiple-scattering paths (full line), or superposing only the paths given in the legend (hatched line); (d) effect of cation vacancies in an Ni-hydroxide layer; (e) effect of attaching a silicate sheet to an Ni–Al hydroxide layer, modeling the formation of a 1 : 1 phyllosilicate; (f) effect of Co-for-Al substitution in a Co hydroxide layer.

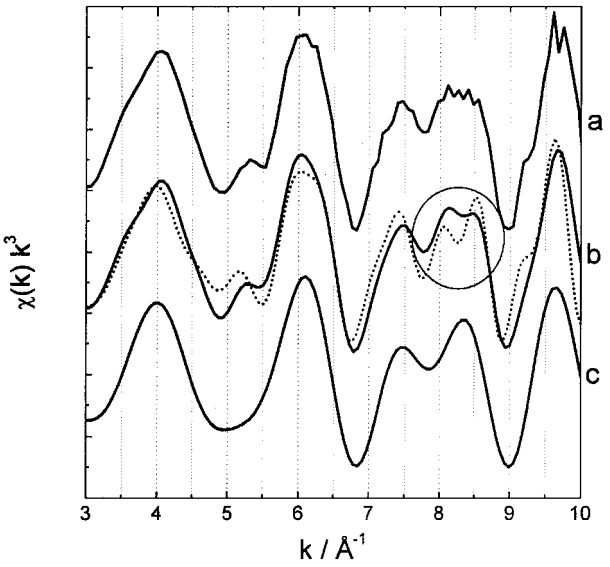

FIG. 6. The $\chi(k)$ spectra of LDH Ni/Al = 1.3 as measured (a) and filtered from the corresponding RSF (see Fig. 3) by Fourier back-transformation. Spectrum b has been filtered from the 1.1- to 6.2-Å region containing the focused multiple-scattering feature at 6 Å, and spectrum c from the 1.1- to 3.4-Å region excluding the feature. For comparison, the filtered $\chi(k)$ function of LDH Ni/Al = 4.3 is shown as a dotted line.

contribute to the overall XAFS spectrum because of weak amplitudes. Due to the hexagonal symmetry and regular metal–metal distances in the hydroxide layer, however, there is a large number of paths with exactly twice the length of the first metal-shell (2×3.08 Å $= 6.16$ Å in the simulations), which strongly enhances their overall amplitude, an effect called focused multiple scattering (25). In fact, all essential features of the LDH spectra could be reproduced by superposition of these focused multiple-scattering paths with the single-scattering paths of the first shells of O, Ni, and Al (Fig. 5c). Although the focused multiple-scattering wave is even stronger without Al substitution, it is only in combination with the Al-dampened single-scattering wave from the first metal shell that the $\chi(k)$-functions show the isolated upward oscillation at 8 Å^{-1} (not shown).

In surface precipitates, Al backscattering may not necessarily stem from Al substituting for Ni in LDH, but from Al in the structure of the sorbent. This would require that the precipitate be in close contact with the surface and that both the precipitate and the sorbent structures be similar enough to generate focused multiple-scattering waves. An example of such a situation would be Ni hydroxide polymers epitaxially growing at the aluminol edges of pyrophyllite or gibbsite, with bidentate bridges connecting the Ni and Al hydroxide sheets. We investigated, therefore, whether this epitaxial growth of a pure Ni hydroxide can be distinguished from an Ni–Al LDH precipitate. A simple representation of this situation shows that a monolayer of Ni octahedra attached to the surface of the aluminol sheet would yield an Ni/Al ratio of 1. A double layer would have a statistical Ni/Al ratio of 2. Assuming a quasi-infinite row of a monolayer of Ni octahedra, the real coordination number for Ni would always be below 2, and the observed coordination number would be close to 1.5 due to the destructive interference of the Al neighbors. As will be shown below, spectra of surface precipitates suggest an Ni/Al ratio of 1, and CN_{Ni-Ni} is above 2. With these constraints, the beat pattern at 8 Å^{-1} can be explained by the formation of Ni–Al LDH only.

Furthermore, we investigated whether cation vacancies, which have been proposed to account for the reduced metal distances observed in surface precipitates (29, 33), would create a similar beat pattern between 8 and 8.5 Å^{-1}. Figure 5d shows that such vacancies dampen the oscillations similar to Al. However, they do not cause the appearance of new beats at 8 and 11.5 Å^{-1}. Thus, vacancies may be present in the structure of the surface precipitates, and may be responsible in part for the contraction of the Me–Me distances, but the characteristic pattern at 8 Å^{-1} unmistakably indicates the presence of Al in hydroxide layers.

In the case of Al- and Si-releasing sorbent phases, formation of Al-containing phyllosilicates is another possibility which has to be addressed (34, 56, 57). The FEFF calculations show that the attachment of one silicate sheet slightly enhances the oscillations at 7.5 and 8.5 Å^{-1}, but not the 8 Å^{-1} beat (Fig. 5e). The overall effect is identical to that of an increasing Ni/Al ratio (Fig. 5b). The attachment of two Si sheets (simulation of a 2 : 1 phyllosilicate) caused the beat pattern to completely disappear. Due to the counteracting effect of Al and Si, the simulated XAFS spectrum of a 1 : 1 Ni/Al phyllosilicate with an Ni/Al ratio of 0.75 would look very similar to the simulated spectrum of an Ni–Al LDH with an Ni/Al ratio of 1. Previous research has shown, however, that Ni/Al ratios in double hydroxide layers are restricted to the range above 1 (39, 58). Therefore, a strong beat pattern at 8 Å^{-1} is incompatible with a phyllosilicate. This deduction is consistent with the fact that XAFS spectra of Ni and Co phyllosilicates do not show the beat pattern at 8 Å^{-1} even when they contain Al (34).

In conclusion, the characteristic beat pattern at 8 Å^{-1} seems to be a unique fingerprint of Ni–Al LDH. In order to test whether a similar beat pattern would allow for the detection of Co–Al LDH, all of the XAFS simulations described above were repeated for Co, using a slightly enlarged structure of lizardite to account for the slightly larger Co^{2+}. The simulated XAFS spectra were identical to those of the Ni structures, except that the phase was shifted by 0.2 Å^{-1} toward lower values due to the larger atomic distances (Fig. 5f). Therefore, the beat pattern may also be used to unequivocally identify Co–Al LDH.

XAFS Analysis of Ni Surface Precipitates

In order to study the influence of different chemical compositions and structures of sorbent phases on the type of Ni surface precipitate forming, we reacted pyrophyllite, gibbsite, talc, and amorphous silica with Ni at pH 7.5. A description of the samples, including Ni sorbed from solution and Al, Si, and Mg released into solution, is given in Table 3. The RSFs of all Ni-reacted sorbents show a strong contribution from metal back-scattering, confirming the formation of three-dimensional Ni precipitates

TABLE 3
Ni Sorption Data on Various Minerals

Sorbent	Reaction time	Ni sorbed (mg g^{-1})	Ni sorbed (μmol m^{-2})	Al in solution (mmol L^{-1})	Si in solution (mmol L^{-1})	Mg in solution (mmol L^{-1})
Pyrophyllite	2 h	5.1	0.9	<0.01	0.18	0.00
Pyrophyllite	1 month	17.1	3.0	<0.01	0.55	0.00
Pyrophyllite	4 months	17.0	3.0	<0.01	0.56	0.00
Gibbsite	4 months	8.8	1.7	<0.01	0.00	0.00
Talc	4 months	17.2	3.3	<0.01	1.13	0.23
Amorphous silica	1 month	5.5	1.0	<0.01	1.80	0.00

(Fig. 7). The $\chi(k)$ spectra of precipitates forming in the presence of the Al-containing minerals pyrophyllite and gibbsite are very similar to that of Ni–Al LDH (Fig. 3), including the characteristic double oscillation at 8.0 to 8.5 $Å^{-1}$ in the filtered $\chi(k)$ function (Fig. 7). The similar heights of both oscillations indicate an Ni/Al ratio between 1 and 2. The formation of Ni–Al LDH in the presence of pyrophyllite and gibbsite is further substantiated by the R_{Ni-Ni} of 3.05 to 3.06 Å (Table 2). For Ni-reacted talc and amorphous silica, the lack of the beat pattern at 8 $Å^{-1}$, the R_{Ni-Ni} of 3.08 to 3.09 Å, and CN_{Ni-Ni} close to 6 suggest the formation of α-Ni hydroxide (Fig. 7, Table 2).

A time series of Ni-reacted pyrophyllite samples shows an increase of the first metal–shell amplitude from 2 h to 1 month (Fig. 8). After 1 month the amplitude remains constant, in line with the completed uptake of Ni from solution (Table 3). The short-range structure of the precipitate seems to stay constant over time, as is indicated by the R_{Ni-Ni} of 3.06 Å (Table 2) and a similar ligand-field splitting energy (35). The similar height of the double oscillation band indicates that the Ni/Al ratio remains at 1 to 2 within 1 month and 1 year (Fig. 8). After 2 h, the 8 $Å^{-1}$ beat is still weak and the overall features are dominated by the Ni–O backscattering wave. Thus, no estimate of the initial Ni/Al ratio can be made.

In both the talc and the amorphous silica suspensions, high Si concentrations (>1 mmol L^{-1}) potentially could lead to the formation of Ni phyllosilicate (34, 57). The XAFS spectra of these precipitates are, however, more similar in phase and amplitude to α-Ni hydroxide than to Ni silicate (compare Figs. 3

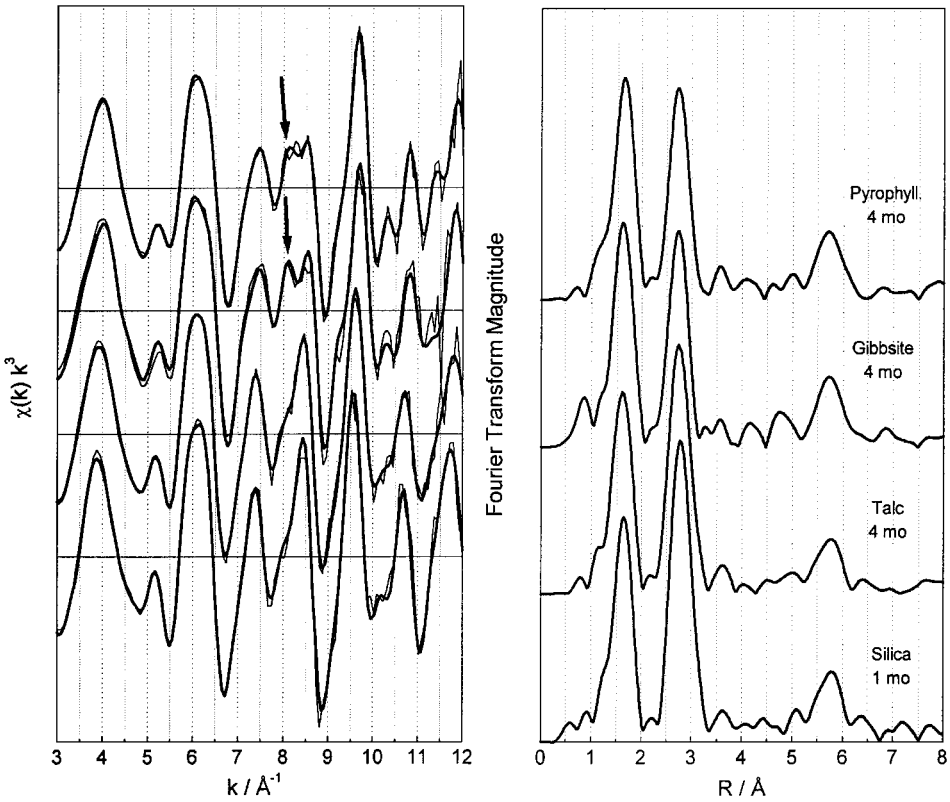

FIG. 7. Experimental $\chi(k)$ functions and RSFs of Ni-reacted sorbents. The $\chi(k)$ functions are given as unfiltered spectra (thin lines) and as back-transforms from $1.1 < R < 6.4$ Å (thick lines).

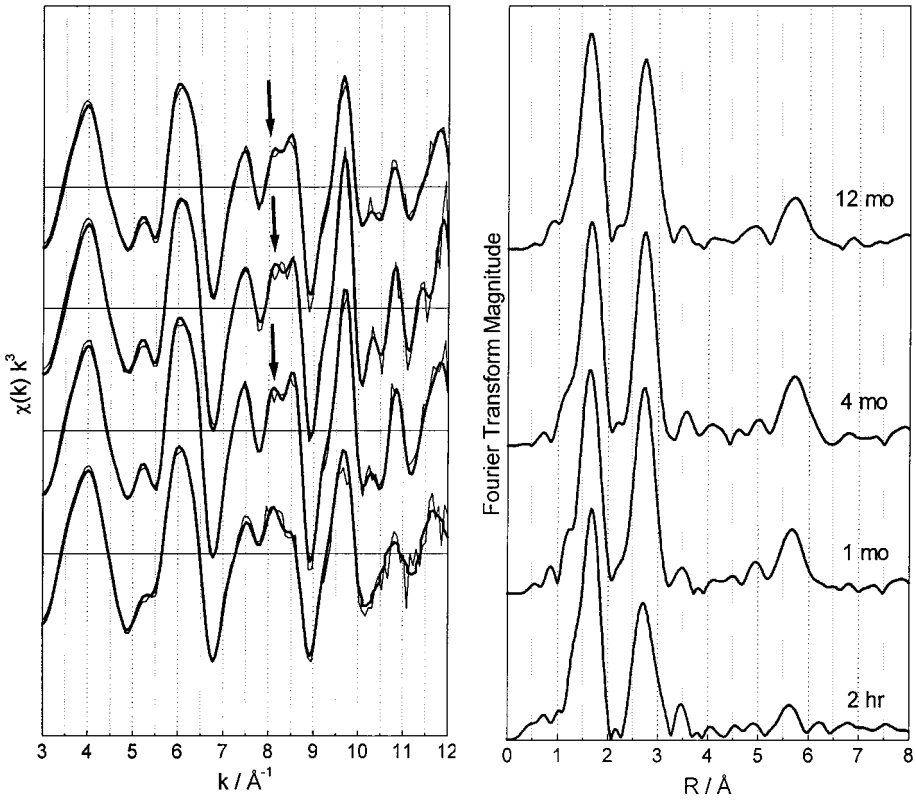

FIG. 8. Experimental $\chi(k)$ functions and RSFs of a time series of Ni-reacted pyrophyllite. The $\chi(k)$ functions are given as unfiltered data (thin lines) and as back-transforms from $1.1 < R < 6.4$ Å (thick lines).

and 7). This is confirmed by the $R_{\text{Ni–Ni}}$ larger than those expected for Ni phyllosilicates, and by the $\text{CN}_{\text{Ni–Ni}}$ below or close to 6 (Table 2). The results indicate, therefore, the formation of α-Ni hydroxide in the talc and the amorphous silica systems, confirming our findings from DRS (35). Note, however, that a phyllosilicate precursor, where polymerized silicate occupies the interlayer space of LDH, cannot be distinguished from LDH by XAFS or DRS (59).

CONCLUSIONS

Using FEFF simulations and experimental XAFS data of model compounds, we demonstrated that a beat at 8 Å^{-1} in $\chi(k)k^3$ spectra of Ni and Co surface precipitates is diagnostic for Ni–Al LDH or Co–Al LDH. Neither the formation of α-type hydroxide with a high degree of cation vacancies nor the formation of Ni- or Co-containing phyllosilicates, nor inner-sphere sorption of multinuclear hydroxide clusters, causes a similar beat pattern. Similar intensities of the diagnostic 8 Å^{-1} beat and of the neighboring 8.5 Å^{-1} beat indicate an Ni/Al ratio of $\approx$1 to 2 for precipitates forming in the presence of pyrophyllite and gibbsite. Absence of the 8 Å^{-1} beat in the spectra of Ni-reacted amorphous silica and talc, in combination with $R_{\text{Ni–Ni}}$ of 3.08 to 3.09 Å and $\text{CN}_{\text{Ni–Ni}}$ below 6, suggests the formation of α-Ni hydroxide. The formation of the two different phases depending on the Al-content of the sorbent phases is in line with our previous study employing DRS (35). As both phases reveal substantially different dissolution kinetics (60), their distinction is important for the prediction of the fate of Ni in the environment.

Using the diagnostic XAFS beat, we re-examined $\chi(k)k^3$ spectra of Co and Ni sorbed onto a range of surfaces that were published within the last decade. The beat pattern is generally visible in the XAFS spectra of Ni- and Co-reacted pyrophyllite, gibbsite, and kaolinite, and of α- and γ-Al_2O_3, at pH from 7.0 to 8.6, surface densities from 0.9 to 5.7 $\mu\text{mol m}^{-2}$, and reaction times from 2 h to 4 months (2, 29–31, 33, 61). This suggests that the formation of LDH is thermodynamically and/or kinetically favored over the formation of α-type hydroxide or phyllosilicates as long as an Al-releasing sorbent is present. In spite of the presence of a potential source of Al, however, α-type Ni or Co hydroxide formed in the presence of montmorillonite (31, 62). The permanent charge sites of these minerals may present a more effective sink for Al than the surface of a growing Ni or Co hydroxide, thus preventing the coprecipitation of LDH. Formation of LDH was also prevented when the solution was highly supersaturated with respect to the pure hydroxide phase (33). In this case, the precipitation proceeds faster than the dissolution of the Al-bearing sorbent phase and/or faster than the diffusion of Al toward the precipitate. Further studies are needed now to determine the thermodynamic properties of the LDH and α-type hydroxide phases which have been identified.

ACKNOWLEDGMENTS

We thank Eef Elzinga (University of Delaware), Robert G. Ford (EPA), and Andre Scheidegger (PSI Switzerland) for fruitful discussions, for valuable suggestions on a first draft of this manuscript, and for XAFS data. This research was funded by USDA, DuPont Co., and the State of Delaware (Delaware Research Partnership Program).

REFERENCES

1. Wersin, P., Charlet, L., Kartheim, R., and Stumm, W., *Geochim. Cosmochim. Acta* **53,** 2787 (1989).
2. Chisholm-Brause, C. J., O'Day, P. A., Brown, G. E., Jr., and Parks, G. A., *Nature* **348,** 528 (1990).
3. Fendorf, S. E., Lamble, G. M., Stapleton, M. G., Kelley, M. J., and Sparks, D. L., *Environ. Sci. Technol.* **28,** 284 (1994).
4. Junta, J. L., and Hochella, M. F., *Geochim. Cosmochim. Acta* **58,** 4985 (1994).
5. McKenzie, R. M., *Aust. J. Soil Res.* **13,** 177 (1975).
6. Burns, V. M., and Burns, R. G., *in* "La genèse des nodules de manganèse," Vol. 289. C. N. d. l. R. Scientifique, Gif-sur-Yvette, 1979.
7. Tessier, A., Rapin, F., and Carignan, R., *Geochim. Cosmochim. Acta* **49,** 183 (1985).
8. Traina, S. J., and Doner, H. E., *Clays Clay Miner.* **33,** 118 (1985).
9. Manceau, A., and Calas, G., *Clay Miner.* **21,** 341 (1986).
10. Borggaard, O. K., *J. Soil Sci.* **38,** 229 (1987).
11. Ainsworth, C. C., Pilon, J. L., Gassman, P. L., and Van Der Sluys, W. G., *Soil Sci. Soc. Am. J.* **58,** 1615 (1994).
12. Gasser, U. G., Juchler, S. J., and Sticher, H., *Soil Sci.* **158,** 314 (1994).
13. Katz, L. E., and Hayes, K. F., *J. Colloid Interface Sci.* **170,** 477 (1995).
14. Brooks, S. C., Taylor, D. L., and Jardine, P. M., *Geochim. Cosmochim. Acta* **60,** 1899 (1996).
15. Hayes, K. F., and Katz, L. E., *in* "Physics and Chemistry of Mineral Surfaces" (P. V. Brady, Ed.), p. 147. CRC Press, Boca Raton, FL, 1996.
16. Bryce, A. L., and Clark, S. B., *Colloids Surf.* **107,** 123 (1996).
17. Larsen, F., and Postma, D., *Environ. Sci. Technol.* **31,** 2589 (1997).
18. Schoonheydt, R. A., Roodhooft, D., and Leeman, H., *Zeolites* **7,** 412 (1987).
19. Bonneviot, L., Legendre, O., Kermarec, M., Olivier, D., and Che, M., *J. Colloid Interface Sci.* **134,** 534 (1990).
20. Clause, O., Gazzano, M., Trifiro, F., Vaccari, A., and Zatorski, L., *Appl. Catal.* **73,** 217 (1991).
21. Kermarec, M., Carriat, J. Y., Burattin, P., Che, M., and Decarreau, A., *J. Phys. Chem.* **98,** 12008 (1994).
22. Verberckmoes, A. A., Weckhuysen, B. M., Pelgrims, J., and Schoonheydt, R. A., *J. Phys. Chem.* **99,** 15222 (1995).
23. Burattin, P., Che, M., and Louis, C., *J. Phys. Chem.* **B101,** 7060 (1997).
24. O'Day, P. A., Parks, G. A., and Brown, G. E., Jr., *Clays Clay Miner.* **42,** 337 (1994).
25. O'Day, P. A., Rehr, J. J., Zabinsky, S. I., and Brown, G. E., Jr., *J. Amer. Chem. Soc.* **116,** 2938 (1994).
26. d'Espinose de la Caillerie, J. B., Kermarec, M., and Clause, O., *J. Am. Chem. Soc.* **117,** 11471 (1995).
27. O'Day, P. A., Chisholm-Brause, C. J., Towle, S. N., Parks, G. A., and Brown, G. E., Jr., *Geochim. Cosmochim. Acta* **60,** 2515 (1996).
28. Scheidegger, A. M., Lamble, G. M., and Sparks, D. L., *Environ. Sci. Technol.* **30,** 548 (1996).
29. Towle, S. N., Bargar, J. R., Brown, G. E., and Parks, G. A., *J. Colloid Interface Sci.* **187,** 62 (1997).
30. Scheidegger, A. M., Lamble, G. M., and Sparks, D. L., *J. Colloid Interface Sci.* **186,** 118 (1997).
31. Scheidegger, A. M., Strawn, D. G., Lamble, G. M., and Sparks, D. L., *Geochim. Cosmochim. Acta* **62,** 2233 (1998).
32. Thompson, H. A., *in* "Department of Geological and Environmental Sciences," p. 117. Stanford University, 1998.
33. O'Day, P. A., Brown, G. E., and Parks, G. A., *J. Colloid Interface Sci.* **165,** 269 (1994).
34. Charlet, L., and Manceau, A., *Geochim. Cosmochim. Acta* **58,** 2577 (1994).
35. Scheinost, A. C., Ford, R. G., and Sparks, D. L., *Geochim. Cosmochim. Acta* **63,** 3193 (1999).
36. Génin, P., Delahaye-Vidal, A., Portemer, F., Tekaia-Elhsissen, K., and Figlarz, M., *Eur. J. Solid State Inorg. Chem.* **28,** 505 (1991).
37. Kamath, P. V., and Therese, G. H. A., *J. Solid State Chem.* **128,** 38 (1997).
38. d'Espinose de la Caillerie, J.-B., Bobin, C., Rebours, B., and Clause, O., *in* "Preparation of Catalysts VI—Scientific Bases for the Preparation of Heterogeneous Catalysts" (G. P. *et al.*, Eds.), p. 169. Elsevier Science, Amsterdam, 1995.
39. Taylor, R. M., *Clay Miner.* **19,** 591 (1984).
40. Grauby, O., Petit, S., Decarreau, A., and Baronnet, A., *Eur. J. Mineral.* **5,** 623 (1993).
41. Mattigod, S. V., Rai, D., Felmy, A. R., and Rao, L., *J. Solution Chem.* **26,** 391 (1997).
42. Lytle, F. W., Sandstrom, D. R., Marques, E. C., Wong, J., Spiro, C. L., Huffman, G. P., and Huggins, F. E., *Nucl. Instrum. Methods. Phys. Res.* **226,** 542 (1984).
43. Ressler, T., *J. Physique IV* **7,** 269 (1997).
44. Rehr, J. J., Mustre de Leon, J., Zabinsky, S., and Albers, R. C., *J. Am. Chem. Soc.* **113,** 5135 (1991).
45. Mellini, C., *Am. Mineral.* **67,** 587 (1982).
46. Gaines, R. V., Skinner, H. C. W., Foord, E. E., Mason, B., and Rosenzweig, A., "Dana's New Mineralogy." Wiley, New York, 1997.
47. Pandya, K. I., O'Grady, W. E., Corrigan, D. A., McBreen, J., and Hoffman, R. W., *J. Phys. Chem.* **94,** 21 (1990).
48. Ehlsissen, K. T., Delahayevidal, A., Genin, P., Figlarz, M., and Willmann, P., *J. Mater. Chem.* **3,** 883 (1993).
49. Schwertmann, U., Friedl, J., and Pfab, G., *J. Solid State Chem.* **126,** 336 (1996).
50. Guggenheim, S., and Eggleton, R. A., *in* "Hydrous Phyllosilicates" (S. W. Bailey, Ed.), Vol. 19, p. 675. Mineralogical Society of America, Chelsea, MI, 1988.
51. Greaves, C., and Thomas, M. A., *Acta Crystallogr.* **B42,** 51 (1986).
52. Mansour, A. N., and Melendres, C. A., *J. Phys. Chem. A* **102,** 65 (1998).
53. Braconnier, J. J., Delmas, C., Fouassier, C., Figlarz, M., Beaudouin, B., and Hagenmuller, P., *Rev. Chim. Miner.* **21,** 496 (1984).
54. Rajamathi, M., Subbanna, G. N., and Kamath, P. V., *J. Mater. Chem.* **7,** 2293 (1997).
55. Manceau, A., and Calas, G., *Am. Mineral.* **70,** 549 (1985).
56. d'Espinose de la Caillerie, J.-B., Kermarec, M., and Clause, O., *J. Phys. Chem.* **99,** 17273 (1995).
57. Depège, C., El Metoui, F.-Z., Forano, C., de Roy, A., Dupuis, J., and Besse, J.-P., *Chem. Mater.* **8,** 952 (1996).
58. Clause, O., Rebours, B., Merlen, E., Trifiro, F., and Vaccari, A., *J. Catal.* **133,** 231 (1992).
59. Ford, R. G., Scheinost, A. C., Scheckel, K. G., and Sparks, D. L., *Environ. Sci. Technol.* **33,** 3140 (1999).
60. Scheckel, K. G., Scheinost, A. C., Ford, R. G., and Sparks, D. L., submitted.
61. Scheidegger, A. M., and Sparks, D. L., *Chem. Geol.* **132,** 157 (1996).
62. Papelis, C., and Hayes, K. F., *Colloids Surf.* **107,** 89 (1996).